Deriving the visual extinction from the trigonometric distance

R. Siebenmorgen[1] and R. Chini[2]

[1] European Southern Observatory, Karl-Schwarzschild-Str. 2, 85748 Garching, Germany, email: Ralf.Siebenmorgen@eso.org
[2] Nicolaus Copernicus Astronomical Center of the Polish Academy of Sciences, Bartycka 18, 00-716 Warsaw, Poland; Ruhr University Bochum, Faculty of Physics and Astronomy, Astronomical Institute (AIRUB), 44780 Bochum, Germany; Universidad Catolica del Norte, Instituto de Astronomia, Avenida Angamos 0610, Antofagasta, Chile

ABSTRACT

Derivation of the viusal extinction from the trigonometric parallax

Key words. ISM: clouds – Stars: early-type – (ISM) dust, extinction

1. Parallax and luminosity distance

The distance D of astronomical objects is a fundamental problem, prompting the exploration of various estimation techniques. The parallax, based on geometric principles, provides the most straightforward approach but is limited to nearby stars. The luminosity distance D_L enables the assessment of distances of many kpc by measuring the apparent stellar brightness and comparing it with the absolute brightness. However, the apparent brightness of stars is usually diminished by an unknown amount of dust.

Traditionally, extinction is determined from the apparent colour of stars in the visible range (e.g. $B - V$), comparing it with the unreddened colour $(B - V)_0$, and multiplying the difference $E(B - V)$ with R_V, the ratio of total-to-selective extinction. The average value of R_V in the Milky Way is ~ 3.1 (Gordon et al. 2023), with extreme values from 2.1 in clouds of high galactic lattitude to 5.6 in dense molecular couds. It should be noted that R_V corresponds to the extinction at infinite wavelengths and is extrapolated from measurements at near-infrared (NIR) wavelegths. The reddening longward of $2.2, \mu$m is more difficult to establish because contamination by either dust or any other emission components of early-type stars might come into play (Siebenmorgen et al. 2018; Deng et al. 2022).

By introducing the photometric equation nearly 100 years ago it was speculated that an additional non-selective or grey extinction term in the form of very large grains A_V^μ – at that time called 'meteoritic' bodies – might exist, which would add another extinction term in Eq. 1

$$V = M_V + 5 \log D - 5 + A_V + A_V^\mu \qquad (1)$$

where M_V is the absolute magnitude of the star and the offset has been arbitrarily set to $A_V^\mu \equiv 0$ (Trumpler 1930).

Meanwhile, micrometre-sized particles have been found in various environments (Sect. 3) providing significant wavelength-independent extinction from the far-UV to the near-infrared. As a consequence, A_V determinations from optical reddening must underestimate the total extinction and thus lead to larger distances. For a few stars it was hypothesized (Krełowski et al. 2015; Siebenmorgen et al. 2020) that incorporating an additional component of large dust grains could reconcile the problem of missing extinction and thus of inaccurate distance estimates; however, this remained unverified due to the lack of a physical model.

In the following we use distances D_{Gaia} obtained from the zero-point corrected parallax following Lindegren et al. (2021) and compare them with the luminosity distances D_L for 33 well-known OB stars. For many stars, our investigation uncovers an inconsistency between both methods; its detection required the unprecedented resolution of the Gaia data release three (Gaia Collaboration et al. 2020). To reconcile the discrepancy in distance, we introduce an additional contribution of grey extinction to the visual ($A_V^\mu \geq 0$, Eq. 1) due to micrometre-sized grains and calibrate their amount with the distance suggested by Gaia.

2. The sample

The inclusion of an additional extinction term necessitates validation through a dust model. For such a test a well-selected sample of reddening curves is crucial. The stars shall have precise photometric measurements, accurate distance determinations, rigorous spectral type classifications and luminosity class identifications, allowing reasonable estimates of the absolute brightness M_V, as well as high-quality reddening curves spanning the entire range from the Lyman limit to infinitely long wavelengths.

In that wavelength range, 820 reddening curves have been published by Valencic et al. (2004); Fitzpatrick & Massa (2007); Gordon et al. (2009), which suffer from various systematic uncertainties. To obtain a high-quality sample, Siebenmorgen et al. (2023) inspected and merged a sample of 186 stars, mainly observed with the Ultraviolet and Visual Echelle Spectrograph (UVES; (Dekker et al. 2000)), complemented by linear polarization data of 215 stars taken from the Large Interstellar Polarization Survey (Bagnulo et al. 2017). From this sample, stars with composite spectra in the IUE/FUSE apertures arising from multiple bright stellar systems were excluded. Likewise, stars were omitted with a photometric variability between space (Kharchenko & Roeser 2009a; Gaia Collaboration et al. 2018a, 2020) and ground-based observations (Valencic et al. 2004) of more than $\sigma(V) = 30$ mmag, $\sigma(B - V) = 30$ mmag, and $\sigma(G) = 11$ mmag. Further, stars that show inconsistent par-

allaxes when comparing data releases two and three from GAIA (Gaia Collaboration et al. 2018a, 2020) were rejected.

The spectral type and luminosity class (SpL) estimates of these stars are important for the determination of the reddening curve and when utilizing M_V for distance estimates (Eq. 1). The SpL were identified by fitting the Gray & Corbally (2014) library to UVES spectra with undetected signatures of binarity or circumstellar line profiles. This provided a precision of half a sub-type/class, which matches the accuracy reached by other studies (Kyritsis et al. 2022; Liu et al. 2019). For the O-stars, it was also confirmed that the SpL classification agrees with that provided by the Galactic O-star survey (Sota et al. 2014). Stars whose classification does not confirm the one used in the reddening curve determination were removed.

In total, 47 stars meet these rejection criteria and provide the highest-quality Milky Way reddening curve sample available today. Most of these stars exhibit single-cloud sightlines, which were identified by analyzing interstellar lines, particularly K I. They show one dominating Doppler component (Siebenmorgen et al. 2020) at a resolving power of $\lambda/\Delta\lambda \sim 75,000$, provided by the high-resolution spectrograph UVES. Dust emission from a circumstellar envelope was not observed in the Spitzer photometry (Siebenmorgen et al. 2018) or WISE $(3 - 22, \mu m)$ imaging. Spectropolarimetry of these sightlines follows the Serkowski curve, elucidated by the dichroic polarization due to differential extinction of magnetically aligned spheroidal grains within the interstellar medium (Bagnulo et al. 2017).

Finally, the accuracy of the trigonometric distance for these stars was verified. For the remaining sample stars, Gaia data release three (Gaia Collaboration et al. 2020) provides accurate astrometric solutions with a renormalized unit weight error (RUWE) of $\sim 0.9 \pm 0.1$, and always less than 1.2 (Luri et al. 2018). The internal error in the Gaia catalogue of the parallax is well below $\sim 5\%$. However, the sample stars are bright with $6 < G\,(\text{mag}) < 10$, for which, following Maíz Apellániz (2022), the uncertainties in the parallax $\sigma(\pi)$ significantly increases. We re-compute the G-mag dependant error in the parallax $\sigma(\pi, G)$ accordingly and consider stars only at a precision of $\sigma(\pi, G))/\pi \lesssim 11\%$.

In total, we examined 33 sightlines towards prominent OB stars within a distance of 2.5 kpc, using the most superior sample of reddening curves and SpL identification currently accessible.

3. The dust model

Our study utilizes a dust model[1] by Siebenmorgen (2023) that aligns with current observational constraints of dust in the diffuse ISM of the Milky Way (Hensley & Draine 2021). It accounts for representative solid phase element abundances and explains accurately phenomena such as wavelength-dependent reddening, extinction, starlight polarization, and the emission of unpolarized and polarized light seen by Planck (Guillet et al. 2018a). Recently, the (sub)millimetre excess emission in the Milky Way has gained an alternative explanation by adjusting the grain emissivity at these wavelengths (Hensley & Draine 2021; Guillet et al. 2018a) in order to avoid micrometre-sized cold dust particles. However, these models fail short resolving the distance discrepancy reported in Sect. 4.

The dust model incorporates three dust populations: 1) nanoparticles of graphite, silicate, and polycyclic aromatic hydrocarbon (PAH), 2) submicrometre-sized spheroidal grains of amorphous carbon and silicate, using the latest optical constants

---

[1] Custom software available at CDS.

for amorphous silicates (Demyk et al. 2022), and 3) micrometre-sized dust particles; the latter component has been labelled by Siebenmorgen et al. (2020) as dark dust (DD).

These micrometre-sized grains are primarily composed of a composite of porous amorphous carbon and silicate particles. Such grains have been detected in scattering light haloes around X-ray sources (Witt et al. 2001; Heinz et al. 2016) and from submillimeter emission of evolved giants (Jura et al. 2001). They preferentially survive the interaction regions between the asymptotic giant branch and the ISM (Maercker et al. 2022).

The presence of very large grains (VLG) in the diffuse ISM is further evidenced by studying flat infrared extinction curves (Wang et al. 2015a,b). This phenomenon can also be explained by very porous, fluffy particles (Krügel & Siebenmorgen 1994) with the degree of porosity constrained through a comparison of optical and submillimetre polarization (Guillet et al. 2018a). Micrometre sized grains have been studied by Voshchinnikov (2004); Krügel (2008) and have been included in other dust models by Ormel et al. (2011); Ysard et al. (2024). Furthermore, micrometre-sized particles from the diffuse ISM were also measured in situ from the Ulysses, Galileo, and Stardust space probes (Landgraf et al. 2000; Westphal et al. 2014; Krüger et al. 2015) and they appear in sightlines connected to the cold ISM (Siebenmorgen et al. 2020).

Micrometre-sized grains absorb a fraction of the interstellar radiation field, ISRF (Mathis et al. 1983). Because these grains are large, they are cold and emit at long wavelengths. Originally very cold (10 K) dust emission was detected in our Galaxy towards high-density regions (Chini et al. 1993) and in non-active galaxies (Chini et al. 1995). Such cold dust was confirmed by ISO (Krügel et al. 1998; Siebenmorgen et al. 1999). More recently, excess emission at 0.5 mm observed by Herschel cannot be explained by a single modified black-body temperature component (Madden et al. 2013; Kennicutt et al. 2011; Rémy-Ruyer et al. 2013); these results were confirmed with ALMA (Galliano et al. 2005) and LABOCA (Galametz et al. 2009) at even longer wavelengths.

4. The distance discrepancy

Trigonometric distances D_{Gaia} were derived from the zero-point corrected parallax π in the Gaia data release three (Gaia Collaboration et al. 2020) following Lindegren et al. (2021). Because distances are always depending on a prior we have verified our results using different methods. For our sample, the simple inverse of the catalogue parallax agrees to typically $1.6 \pm 1.8\,(\%)$ with D_{Gaia} and stays always below 5.5 %. Our distance estimate D_{Gaia} aligns with other probabilistic Gaia distance estimates (Bailer-Jones et al. 2021) to better than $1 - 2\,(\%)$.

The luminosity distance $D_{\text{L}}(A^{\text{Ref}})$ was computed using Hipparcos photometry (Kharchenko & Roeser 2009b); spectral types and luminosity classes are from UVES (Siebenmorgen et al. 2023). Absolute magnitudes M_V were calculated from our SpL and the conversion tables (Bowen et al. 2008; Wegner 2006). The visual extinction A_V^{Ref} was obtained by extrapolation of the reddening curves (Valencic et al. 2004; Fitzpatrick & Massa 2007; Gordon et al. 2009). The errors in $D_{\text{L}}(A^{\text{Ref}})$ primarily arise from systematic uncertainties. We apply the conservative error estimate $\sigma(M_V)$ in M_V following Bowen et al. (2008). The 1σ scatter between M_V of the spectral type and the adjacent ± 0.5 subtype is denoted as σ_{SpT}, the 1σ scatter between M_V of the luminosity class ± 1 luminosity class is denoted as σ_{LC}. To account for an offset between both catalogues we introduce σ_C;
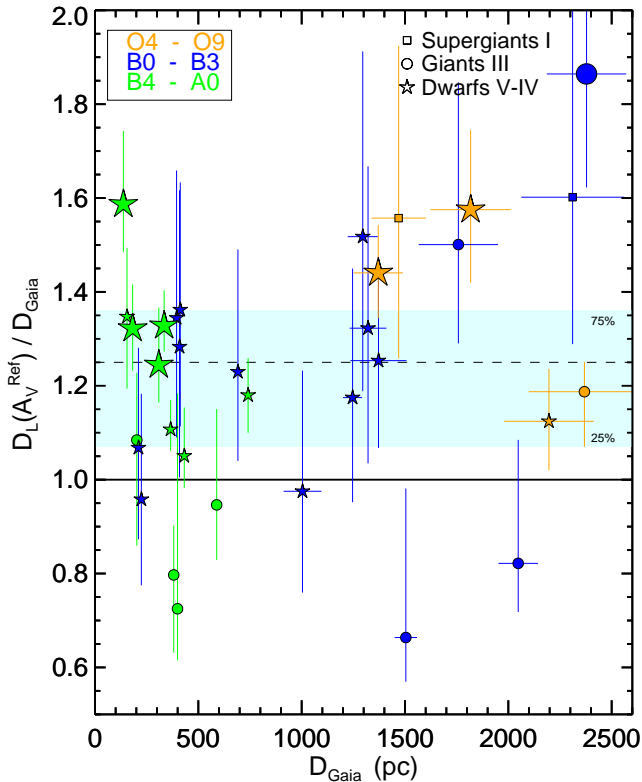
Fig. 1. The distance ratios $D_L(A^{Ref})/D_{Gaia}$ vs. D_{Gaia} for our sample of 33 stars using visual extinction A_V^{Ref} estimates obtained by extrapolation of the reddening (Valencic et al. 2004; Fitzpatrick & Massa 2007; Gordon et al. 2009). Different symbols and colours are used to visually represent the various spectral types and luminosity classes as labelled. Stars with a deviation in the distance ratios from unity that are below 3σ in M_V are shown by small symbols. The shaded area depicts the top and bottom quartiles of the distribution, with the mean indicated by a dashed line.

thus, $\sigma^2(M_V) = \sigma_{SpT}^2 + \sigma_{LC}^2 + \sigma_C^2$. For estimating the error in the luminosity distance we add the photometric error $\sigma(V)$.

Fig. 1 shows the distance ratios $D_L(A^{Ref})/D_{Gaia}$ vs. D_{Gaia} for our sample. For the same star, the luminosity distance $D_L(A^{Ref})$ generally overpredicts the Gaia distance D_{Gaia}. There are no stars with a distance ratio below $D_L(A^{Ref})/D_{Gaia} < 1.25$ detected at 3σ confidence. The distance ratios range between $0.7 \lesssim D_L(A^{Ref})/D_{Gaia} \lesssim 1.9$. The bottom and top quartiles are at 1.09 and 1.37, which underlines the overprediction in $D_L(A^{Ref})$. A dependency of $D_L(A^{Ref})$ on the spectral types and luminosity classes is not observed. We emphasize that stars of identical spectral types show deviations in opposite directions which excludes any systematic offsets in M_V (Table 1). Therefore, we interpret this discrepancy as to arise from an underestimate of A_V^{Ref}.

Recent investigations (Shull & Danforth 2019) were still not able to detect any discrepancy within the errors of the Gaia data release two (Gaia Collaboration et al. 2018b); this could only be brought to light utilizing the unprecedented resolution of the Gaia data release three.

5. Absolute reddening

In the following, we calculate the amount of visual extinction, denoted by A_V^*, which is necessary to align D_L with D_{Gaia} using the photometric equation in the form
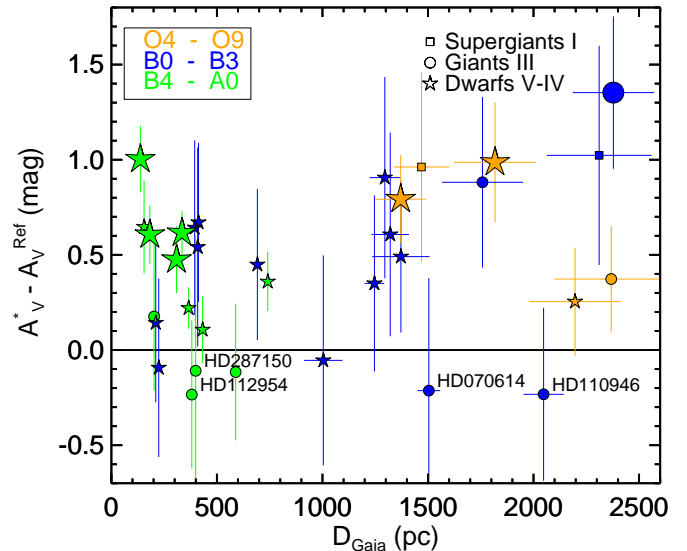

Fig. 2. Comparison of previous and our estimates of the visual extinction. The difference of $A_V^{Ref} - A_V^{Ref}$ with error bars (Eq. 3) is shown for our sample along the trgometric disance D_{Gaia}. Notation as in Fig. 1, with different spectral types and luminosity classes as labelled.

$$A_V^* = V - M_V - 5 \log D_{Gaia} + 5 . \qquad (2)$$

with error estimate

$$\sigma(A_V^*)^2 = \sigma(V)^2 + \sigma(M_V)^2 + \left(\frac{5}{\log 10} \frac{\sigma(\pi, G)}{D_{Gaia}} \right)^2 \qquad (3)$$

In Fig. 2 we compare the difference between our estimate of the visual extinction A_V^* (Eq. 2) and the estimate A_V^{Ref}, which was obtained by extrapolation of the reddening (Valencic et al. 2004; Fitzpatrick & Massa 2007; Gordon et al. 2009). Similar to Fig. 1 and irrespective of the SpL, the latter estimate A_V^{Ref} exhibits a general underestimate of about half a magnitude when compared to A_V^*.

The optical depth $\tau_V = A_V^*/1.086$ is related to the column densities of nanoparticles and submicrometre-sized particles N_n and to the column density of micrometre-sized grains N_μ; the corresponding mass extinction cross-section K_n and K_μ (g/cm^3) are based on the dust model (Siebenmorgen 2023):

$$\tau_V = N^n K_V^n + N^\mu K_V^\mu < \|E(H)\| /1.086 . \qquad (4)$$

The extinction cross-section (Draine 2003; Voshchinnikov 2004; Krügel 2008) diminishes at infinite wavelengths, i.e. $K(\infty) = 0$. To prevent negative optical depths, we assume that the reddening at infinite wavelengths is smaller than in the H-band, hence $A_V^* = -E(\infty) > -E(H)$. The reddening $E(B - V) = 1.086 (\tau_B - \tau_V)$ provides a second constraint:

$$\tau_B - \tau_V = N^n (K_B^n - K_V^n) + N^\mu (K_B^\mu - K_V^\mu) . \qquad (5)$$

These two equations enable us to derive the specific mass of each component, specifically $m_n = N_n/(N_n + N_\mu)$ of the nano- and submicrometre-sized grains and $m_\mu = N_\mu/(N_n + N_\mu)$ of the micrometre-sized particles. Notably, our approach for computing A_V^* is validated through a fit to the observed reddening curve using our dust model and obviates need for the extrapolated parameter $R_V = A_V/E(B - V)$.

Table 1. Data supporting Fig. 1 and Fig. 5.

1	2	3	4	5	6	7	8	9	10	11
Star	Ref	SpL	V	M_V	$D_L(A_V^{\text{Ref}})$	D_{Gaia}	$D_L(A_V^*)$	A_V^{Ref}	A_V^*	A_V^μ
			(mag)	(mag)	(pc)	(pc)	(pc)	(mag)	(mag)	(mag)
HD027778	G	B3V	6.33	$-1.52^{+0.39}_{-0.44}$	225^{+45}_{-41}	210 ± 3	210	1.09	1.23 ± 0.42	0.23
HD037903	G	B2V	7.84	$-2.28^{+0.46}_{-0.46}$	531^{+124}_{-100}	395 ± 10	395	1.49	2.13 ± 0.46	0.79
HD038023	F	B3V	8.87	$-1.52^{+0.39}_{-0.44}$	562^{+112}_{-103}	413 ± 7	413	1.64	2.31 ± 0.42	0.80
HD046223	V	O4V	7.31	$-5.65^{+0.13}_{-0.13}$	1974^{+126}_{-118}	1371 ± 120	1370	1.48	2.27 ± 0.23	0.85
HD054439	F	B1V	7.71	$-3.04^{+0.50}_{-0.53}$	979^{+254}_{-212}	1004 ± 92	1004	0.80	0.75 ± 0.55	0
HD062542	G	B5V	7.99	$-1.21^{+0.12}_{-0.09}$	405^{+23}_{-16}	366 ± 5	366	1.16	1.38 ± 0.11	0.40
HD070614	F	B3III	9.29	$-2.85^{+0.85}_{-0.33}$	998^{+477}_{-139}	1504 ± 54	**1101**	2.14	1.93 ± 0.59	0.20
HD091824	F	O7V	8.15	$-4.90^{+0.21}_{-0.21}$	2863^{+293}_{-266}	1817 ± 194	1817	0.77	1.76 ± 0.32	0.98
HD092044	F	B1Ib	8.31	$-5.95^{+0.59}_{-0.46}$	3702^{+1153}_{-713}	2311 ± 248	2311	1.42	2.44 ± 0.58	1.09
HD093222	G	O6III	8.10	$-5.90^{+0.05}_{-0.20}$	2812^{+66}_{-243}	2368 ± 270	2368	1.76	2.13 ± 0.28	0.76
HD101008	F	B0III	9.16	$-5.00^{+0.42}_{-0.30}$	4434^{+951}_{-567}	2378 ± 192	2378	0.93	2.28 ± 0.40	1.27
HD108927	F	B5V	7.77	$-1.21^{+0.12}_{-0.09}$	444^{+25}_{-18}	335 ± 7	334	0.74	1.36 ± 0.12	0.55
HD110336	F	B8V	8.64	$-0.49^{+0.20}_{-0.14}$	384^{+38}_{-25}	309 ± 3	309	1.21	1.69 ± 0.18	0.41
HD110946	F	B2III	9.18	$-3.55^{+0.60}_{-0.29}$	1683^{+537}_{-207}	2048 ± 95	**1873**	1.60	1.37 ± 0.45	0
HD112607	F	B5III	8.10	$-1.48^{+0.42}_{-0.29}$	557^{+120}_{-69}	589 ± 15	588	0.85	0.73 ± 0.36	0
HD112954	F	B9III	8.39	$-0.77^{+0.27}_{-0.50}$	304^{+40}_{-63}	381 ± 5	**338**	1.75	1.52 ± 0.39	0
HD129557	V	B1V	6.09	$-3.04^{+0.50}_{-0.53}$	525^{+136}_{-113}	409 ± 17	409	0.53	1.07 ± 0.52	0.47
HD146284	F	B9III	6.71	$-0.77^{+0.27}_{-0.50}$	219^{+29}_{-45}	202 ± 3	202	0.77	0.95 ± 0.39	0.21
HD146285	F	B9IV	7.93	$0.10^{+0.22}_{-0.26}$	209^{+23}_{-24}	155 ± 2	155	1.23	1.88 ± 0.25	0.69
HD147196	F	B8V	7.04	$-0.49^{+0.20}_{-0.14}$	218^{+21}_{-14}	137 ± 1	137	0.84	1.84 ± 0.18	0.96
HD148594	F	B7V	6.89	$-0.67^{+0.15}_{-0.15}$	241^{+17}_{-16}	182 ± 2	182	0.65	1.26 ± 0.16	0.60
HD152245	V	B0.5III	8.39	$-4.80^{+0.45}_{-0.32}$	2639^{+600}_{-358}	1758 ± 192	1758	1.08	1.96 ± 0.45	1.00
HD152249	G	O9Ia	6.38	$-7.00^{+0.46}_{-0.46}$	2288^{+535}_{-434}	1469 ± 131	1469	1.58	2.54 ± 0.50	1.12
HD170634	F	B8V	9.85	$-0.49^{+0.20}_{-0.14}$	454^{+45}_{-29}	432 ± 6	432	2.05	2.16 ± 0.18	0.16
HD170740	F	B2V	5.75	$-2.28^{+0.46}_{-0.46}$	215^{+50}_{-41}	224 ± 12	224	1.37	1.28 ± 0.47	0.08
HD185418	G	B0.5V	7.49	$-3.55^{+0.42}_{-0.36}$	850^{+180}_{-131}	692 ± 24	692	1.39	1.84 ± 0.40	0.51
HD287150	F	A1III	9.26	$0.73^{+1.06}_{-0.36}$	289^{+183}_{-44}	399 ± 5	**304**	1.22	1.11 ± 0.71	0.05
HD294304	F	B6V	10.05	$-0.89^{+0.14}_{-0.15}$	874^{+58}_{-59}	741 ± 18	741	1.23	1.59 ± 0.16	0.38
HD303308	V	O6V	8.12	$-5.20^{+0.19}_{-0.19}$	2469^{+220}_{-202}	2196 ± 217	2196	1.36	1.61 ± 0.29	0.32
HD315021	F	B0V	8.57	$-3.85^{+0.34}_{-0.34}$	1719^{+287}_{-246}	1372 ± 136	1372	1.24	1.73 ± 0.40	0.62
HD315023	F	B2V	10.03	$-2.28^{+0.46}_{-0.46}$	1464^{+342}_{-277}	1246 ± 46	1246	1.48	1.83 ± 0.46	0.50
HD315024	F	B1V	9.63	$-3.04^{+0.50}_{-0.53}$	1966^{+510}_{-425}	1295 ± 73	1295	1.20	2.11 ± 0.53	1.04
HD315032	F	B1V	9.18	$-3.04^{+0.50}_{-0.53}$	1747^{+453}_{-378}	1321 ± 89	1321	1.01	1.62 ± 0.54	0.70

Notes: Reddening curves (column 2) by F (Fitzpatrick & Massa 2007), G (Gordon et al. 2009), V (Valencic et al. 2004) , V-band (column 4) by Kharchenko & Roeser (2009b), SpL (column 3) by Siebenmorgen et al. (2023) with associated M_V (column 5) by Bowen et al. (2008); Wegner (2006), luminosity distance $D_L(A_V^{\text{Ref}})$ (column 6) using extrapolated A_V^{Ref} (column 9) estimated by the same authors of the reddening curves, trigonometric distance D_{Gaia} (column 7) from the zero-point corrected parallax π in the Gaia data release three (Gaia Collaboration et al. 2020) following Lindegren et al. (2021) with G-mag dependant error following Maíz Apellániz (2022), luminosity distance $D_L(A_V^*)$ (column 8) utilizing our new estiamte of A_V^* (column 10), $D_L(A_V^*)$ is highlighted in bold when deviating from D_{Gaia}, and the contribution to the visual extinction by micrometre-sized grains A_V^μ (column 11) when utilizing the DD model by Siebenmorgen (2023).

6. Fitting reddening curves

The methodology for calculating the wavelength-dependent extinction cross-section $K(\lambda)$ for partially aligned and wobbling spheroidal grains, nanoparticles, and PAH, from the optical constants of dust materials, is outlined in Siebenmorgen (2023). The

Table 2. Model parameters for sightlines without significant contribution from micrometre-sized grains.

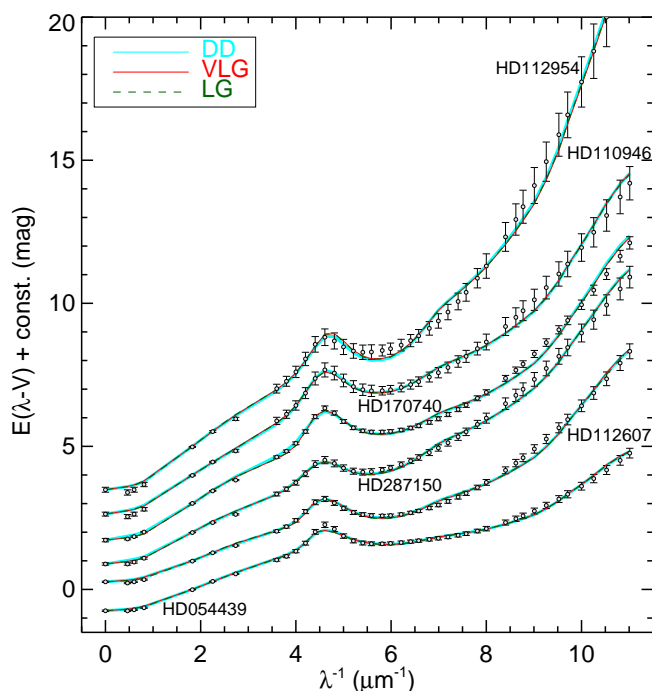| Star	m_{Si} (%)	m_{vSi} (%)	m_{aC} (%)	m_{vgr} (%)	m_{PAH} (%)	q	r_{Si}^+ (nm)	r_{aC}^+ (nm)	Models
HD 054439	58	19	17	5	1	2.6	201	257	DD, VLG
″	55	18	20	5	2	2.7	192	245	LG
HD 110946	40	27	26	4	3	2.8	183	257	DD, VLG
″	39	28	26	4	2	2.8	174	233	LG
HD 112607	51	33	9	5	2	2.4	222	344	DD, VLG
″	50	33	10	5	2	2.4	211	245	LG
HD 112954	40	41	12	4	2	2.6	233	245	DD, VLG, LG
HD 170740	49	23	12	4	3	2.6	233	211	DD, VLG, LG
HD 287150	31	33	23	2	4	3.0	233	211	DD, VLG, LG

Fig. 3. The absolute reddening curves $E(\lambda - V)$ of sightlines without significant contributions from micrometre-sized grains, shifted by an offset for better visibility. Data points (circles) cover the range $0.09 - 2.2\mu$m and are complemented at infinite wavelengths by $-A_V^*$ (Eq.1, Table 1). The best fit, which almost overlapp, is shown for three dust models: DD (cyan), VLG (red), and LG (dashed green) with parameters provided in Table 2.

normalized reddening curves $E(\lambda - V)/E(B - V)$ for the sample are observed spectroscopically between $0.09 - 0.27\mu$m with IUE/FUSE satellites and in the UBV- and JHK-bands with references listed in column 2 of Table 1. These curves are transformed into absolute reddening that are used in this work by multiplying them with the corresponding reddening $E(B - V)$ provided in those same references. The extrapolated reddening at infinitely long wavelengths is substituted with the visual extinction A_V^*, derived from Eq. 2, and are specified in column 10 of Table 1. By adjusting grain sizes and abundances within the three populations, we achieve the best fit for the absolute reddening curve of each star, surpassing previous models that solely addressed relative reddening or extinction curves.

To achieve the optimal fits for the reddening curves, we employ the vectorized minimum χ^2 fitting procedure by Siebenmor-

gen (2023). In this context, the specific masses of various particles are treated as free parameters: the micrometre-sized grains (m_μ), submicrometre-sized particles composed of amorphous silicates (m_{Si}) and carbon (m_{aC}), and the nanoparticles of silicates (m_{vSi}), graphite (m_{vgr}), and PAH (m_{PAH}). These fits adhere to the constraint of cosmic solid phase abundances, ensuring

$$\frac{[C]}{[Si]} < 5.2 . \tag{6}$$

Fine-tuning of the fits to the 2175 Å bump involves allowing the central wavelength (x_0) and damping constant (γ) of the Lorentzian profiles of PAH absorption cross-section to remain free. In the framework of the power-law dust size distribution, the exponent (q) and upper radii for micrometre-sized (r_μ^+), submicrometre-sized silicate, and carbon grains (r_{Si}^+, r_{aC}^+). The specific mass of micrometre-sized particles are given by Eq. 2 and their contribution to the visual extinction, A_V^μ are listed in column 11 of Table 1. In total ten adjustable parameters are treated. We label these as DD - models.

Previous dust models of the diffuse interstellar medium adopt different size distributions (Mathis et al. 1977; Greenberg & Chlewicki 1983) and explain the mean dust extinction of the Milky Way (Fitzpatrick & Massa 2007; Siebenmorgen et al. 2023) by adopting paricles at radii $(r_{aC}^+, r_{Si}^+) \lesssim 250$ nm, e.g. Desert et al. (1990); Mathis & Whiffen (1989); Siebenmorgen & Krügel (1992); Dwek et al. (1997); Weingartner & Draine (2001); Draine & Li (2001, 2007); Das et al. (2010); Draine & Fraisse (2009); Compiègne et al. (2011); Siebenmorgen et al. (2014); Voshchinnikov et al. (2016); Jones et al. (2017); Guillet et al. (2018b). We label these as large-grain (LG) - models. Additionally, we established dust models that omit the micrometre-sized dust component ($m_\mu = 0$) and instead employ a continuous power-law size distribution for the particles with radii (r_{aC}^+, r_{Si}^+) as free parameters extending up to several micrometres. We label these as very large grain (VLG) - model. The LG and VLG entail eight free parameters.

6.1. Sightlines without micrometre-sized grains

The reddening curves of four out of the 33 sightlines are fitted without considering a contribution from micrometre-sized grains ($A_V^\mu = 0$), while the two sightlines towards HD170740 and HD287150 show marginal contributions $A_V^\mu < 0.08$ mag, (Table 1). For these stars, the luminosity distance underestimates the trigonometric distances $D_L(A_V^*) < D_{Gaia}$. Their reddening curves are displayed in Fig. 3. They exhibit variations in the 2175Å bump and resemble the spectrum, ranging from flat (HD054439)
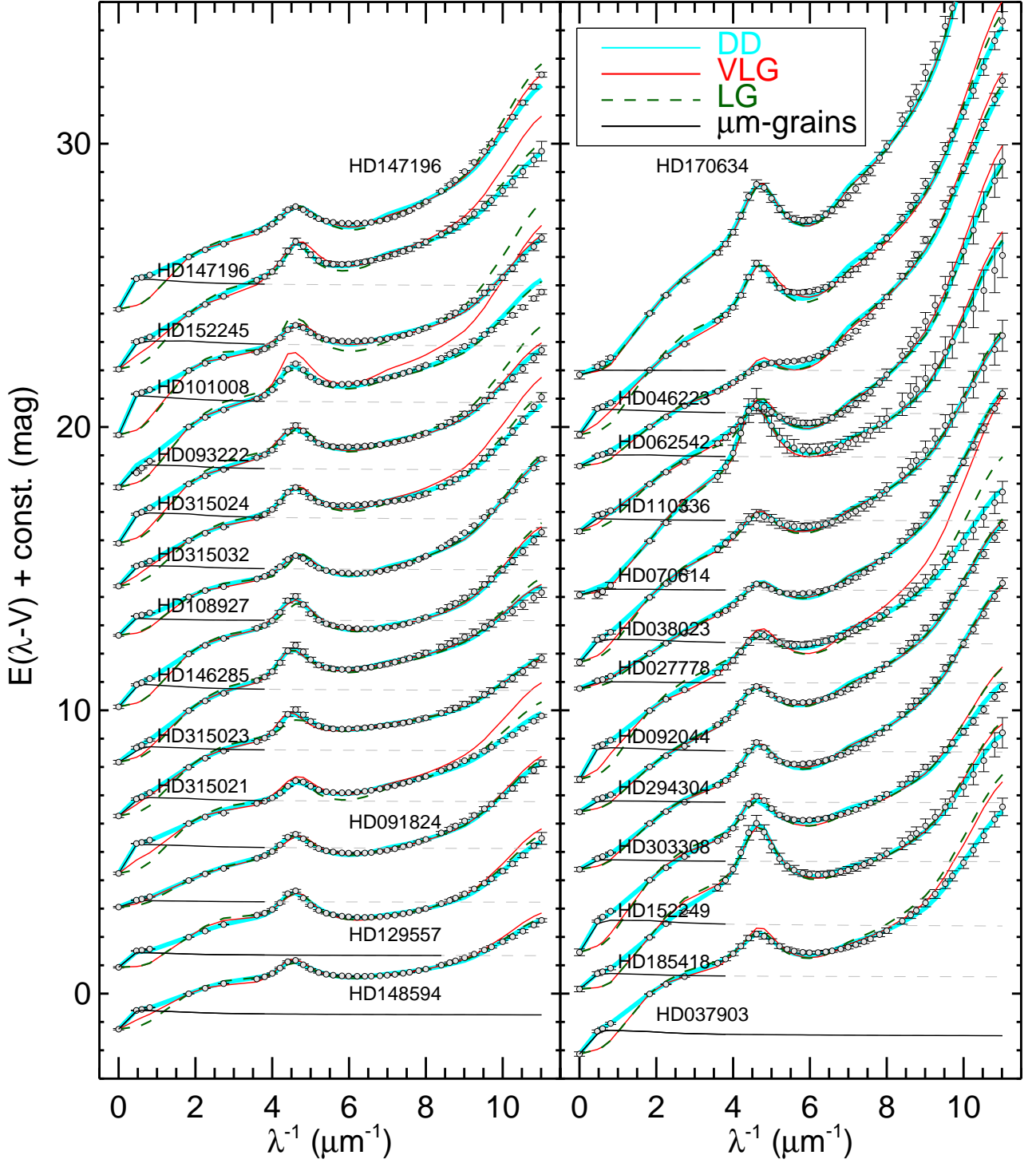
Fig. 4. The absolute reddening curves $E(\lambda - V)$ of sightlines with contributions from micrometre-sized grains ($A_V^\mu \gtrsim 0.2$ mag), shifted by an offset for better visibility. Data points (circles) cover the range $0.09 - 2.2\mu$m and are complemented at infinite wavelengths by $-A_V^*$ (Eq.1, Table 1). The best fit among the three dust models: DD (cyan) with contributions from micrometer-sized grains (black), VLG (red), and LG (dashed green) is shown, with model parameters listed in Table 3. Notable is the dominance of the micrometer-sized grains in the NIR reddening, which are not accounted for by the LG and VLG models, respectively.

to steep rising (HD112954) reddening in the far UV towards the Lyman limit. The reddening data are equally well-fitted by each of the three dust models DD, VLG, and LG. The best-fit parameters are provided in Table 2. For the same star they vary

marginal, which is primarily due to the constrained upper grain radii of $(r_{aC}^+, r_{Si}^+) \lesssim 250$ nm used by the LG model.

Table 3. Parameters of the DD and VLG absolute reddening curve models for sightlines with a significant contribution of micrometre-sized grains.

Star	m_μ (%)	m_{Si} (%)	m_{vSi} (%)	m_{aC} (%)	m_{vgr} (%)	m_{PAH} (%)	q	r_{Si}^+ (nm)	r_{aC}^+ (nm)	r_μ^+ (μm)	χ_r^2	Model
HD 027778	34	31	21	8	3	4	2.4	222	211	2.2	1.0	DD
"	–	47	27	19	3	4	2.7	245	461		6.8	VLG
HD 037903	59	17	10	11	2	3	2.2	245	201	1.3	0.2	DD
"	–	43	20	30	4	3	2.3	328	245		89	VLG
HD 038023	54	22	12	9	2	3	2.4	222	201	1.7	0.2	DD
"	–	46	19	30	2	3	2.6	257	344		4.9	VLG
HD 046223	68	17	10	3	1	4	2.3	233	211	3.6	1.1	DD
"	–	47	22	23	2	5	2.6	297	618		16	VLG
HD 062542	30	30	29	7	2	2	2.6	233	211	1.3	1.3	DD
"	–	46	38	11	3	3	2.5	270	270		37	VLG
HD 070614	17	53	15	9	4	3	2.4	233	233	1.6	0.3	DD
"	–	64	18	11	5	3	2.4	233	233		1.1	VLG
HD 091824	92	4	2	2	0	2	2.4	222	211	6.4	1.7	DD
"	–	50	12	35	1	3	2.4	328	1007		99	VLG
HD 092044	91	4	2	2	0	6	2.8	257	211	14.0	0.2	DD
"	–	41	22	30	2	6	2.6	344	439		46	VLG
HD 093222	60	18	7	13	2	2	2.6	270	211	1.6	4.2	DD
"	–	45	18	32	4	2	2.6	361	233		99	VLG
HD 101008	90	6	2	2	1	1	2.1	257	222	4.1	0.3	DD
"	–	65	10	20	2	2	2.3	361	312		99	VLG
HD 108927	91	5	2	1	1	2	1.8	270	211	9.0	2.0	DD
"	–	62	18	14	4	2	2.0	380	158		99	VLG
HD 110336	74	11	9	3	1	4	2.0	222	211	6.4	0.4	DD
"	–	35	29	27	4	6	2.4	257	461		26	VLG
HD 129557	74	19	4	0	1	4	1.7	257	158	2.4	0.3	DD
"	–	76	13	1	3	6	1.2	270	158		99	VLG
HD 146284	40	31	14	10	3	4	2.0	233	201	1.5	0.2	DD
"	–	48	18	25	4	4	2.3	257	418		6.3	VLG
HD 146285	61	22	6	8	2	4	1.7	257	201	1.3	0.2	DD
"	–	53	11	27	3	6	1.9	297	257		36	VLG
HD 147196	77	11	7	3	0	8	1.7	233	222	2.1	1.8	DD
"	–	42	21	27	1	9	1.9	312	245		99	VLG
HD 148594	71	19	5	4	1	2	1.8	245	192	1.5	0.2	DD
"	–	53	8	35	2	2	2.2	328	870		80	VLG
HD 152245	70	14	7	7	1	3	2.4	201	174	1.8	0.2	DD
"	–	49	12	33	2	4	2.7	344	959		18	VLG
HD 152249	71	14	6	8	1	2	2.6	222	192	2.2	0.7	DD
"	–	47	15	33	3	2	2.5	270	297		99	VLG
HD 170634	90	5	3	1	0	6	2.3	257	201	104	0.9	DD
"	–	45	32	14	2	7	2.3	257	211		2.9	VLG
HD 185418	48	36	8	2	0	9	2.3	257	222	2.1	0.2	DD
"	–	72	14	5	1	8	2.1	257	222		10	VLG
HD 294304	66	15	9	8	1	4	2.9	257	201	7.1	0.6	DD
"	–	44	22	26	3	4	3.0	297	270		19	VLG
HD 303308	44	30	15	7	1	5	2.4	257	211	2.8	0.8	DD
"	–	53	23	18	1	5	2.6	270	297		12	VLG
HD 315021	58	26	5	9	1	2	2.6	270	201	1.6	0.1	DD
"	–	54	7	36	1	3	2.6	297	751		5.5	VLG
HD 315023	45	30	7	15	2	3	2.7	297	211	1.2	0.2	DD
"	–	52	10	33	2	3	2.7	297	328		6.0	VLG
HD 315024	72	13	5	7	1	3	2.4	245	201	1.6	0.2	DD
"	–	50	11	32	3	3	2.5	344	297		64	VLG
HD 315032	66	16	7	8	2	2	2.3	233	201	1.6	0.2	DD
"	–	47	15	33	3	2	2.4	297	649		24	VLG

Notes: The χ^2 reduced by the degree of freedom is truncated to $\chi_r^2 \lesssim 99$.

6.2. Sightlines with micrometre-sized grains

For most (80%) of the sanple, 27 out of 33 stars, we find a significant contribution from micrometre-sized grains with $A_V^\mu >$ 0.2 mag (Table 1). The comparison between the fits to the absolute reddening curves by the LG, VLG, and DD models for these sightlines are displayed in Fig. 4 and the best fit parameters of the DD and VLG models are given in Table 3.

The LG models, which do not treat micrometre-sized grains, often do not fit the data, see green curves in Fig. 4. They fail to account for the far UV (e.g. HD 152245) and in all cases, including HD 170634, gravely underestimates the near IR reddening. Even for some stars (e.g. HD046223, HD 092044, HD 093222, HD 185418, ...) the LG models do not account for the reddening in the U and B bands.

The VLG models include micrometre-sized grains and fit the reddening data for most sightlines better than the LG model. Noticeable deficiencies of the VLG models in fitting the data are prominent, see red curves in Fig. 4. In some cases (e.g. HD 046223, HD091824, HD 092044, ...) the VLG model approches the NIR reddening closer than the LG models. However, also the VLG models underestimate the reddening in the *JHK* bands significantly for all these sightlines. Deviations of the VLG models from the data are visible in the 2175Å bump (e.g. HD 101008) and in the far UV range (e.g. HD 037903, HD 0920444). Overall these deficits of the VLG models are reflected in the reduced χ_r^2 (Table 3), which for all stars are larger than one at typically scatter around $\chi_r^2 = 18 \pm 180$.

The DD models fit the reddening curves at $\chi_r^2 = 0.3 \pm 0.7$ and never exceeds 4.2, see cyan curves in Fig. 4. The largest deviation of the DD model is encountered in the far UV reddening towards HD 093222. For the other 26 stars the overall match is better than $\chi_r^2 < 2$ and in particluar the near IR/optical data are fit well.

7. Distance unification

Correcting the distance discrepancy is not feasible through arbitrary adjustments to commonly used literature values in M_V and $A_V^{Ref} = R_V/E(B - V)$ inserted in Eq. 1. Several stars with identical SpL show different distance ratios and thus would require different adjustments in M_V to reach $D_L = D_{Gaia}$. The uncertainties in M_V range from 0.25 to 0.5 (mag). However, for stars with $D_L/D_{Gaia} \gtrsim 1.2$, modifications of $M_V > 0.5$ mag, – typically 0.8 ± 0.3 mag – would be necessary to align D_L with D_{Gaia}. Similarly, the typical error in $E(B - V)$ is around 0.03 mag; for stars with $D_L/D_{Gaia} \gtrsim 1.2$, modifications of $0.14 \lesssim E(B-V) \lesssim 0.56$ mag would be required to achieve distance unification. Consequently, we retain $E(B - V)$ and substitute the extrapolated R_V parameter with our dust model, utilizing Eqs. 2-5. In this manner, we achieve a consistent estimate of the absolute reddening $E(\lambda - V)$ going beyond previous models that only discussed normalized reddening $E(\lambda - V)/E(B - V)$.

Fig. 5 shows the corrected distance ratios $D_L(A_V^*)/D_{Gaia}$ vs. D_{Gaia} for our sample, where $D_L(A_V^*)$ denotes the luminosity distance derived with our newly determined A_V^* values from Eq. 2. The new luminosity distances $D_L(A_V^*)$, agree with D_{Gaia} within $0.75 < D_L(A_V^*)/D_{Gaia} \lesssim 1$ and show a 1σ scatter of 6 % around a median of one. The four stars with $D_L(A_V^*) > D_{Gaia}$ still agree within their errors with equal distances $D_L(A_V^*) = D_{Gaia}$. For 29 out of 33 stars both distances agree within 2%. Their scatter of the distance ratio is reduced by a factor 40 when compared to the literature values $D_L(A_V^{Ref})$, which are, for ease of comparison, also shown in Fig. 5.

The reliability of our A_V^* estimate (Eq. 2) is validated through fitting the absolute reddening curve across the entire observed wavelength range using our dust model, which incorporates micrometre-sized grains. Models that incorporate the continuation of the dust size distribution to micrometres for the large carbon and silicate grains but overlook dark dust frequently exhibit discrepancies in the far UV and fail to align with the data in the NIR (Fig. 3).

The micrometre-sized dust population typically contributes to typically 30 ± 17.5 %, comprising less then a third of the total extinction A_V^* (Table 1). The amount of this dust component depends on the environmental condition and chemical composition of the clouds and varies along different sightlines (Table 3).
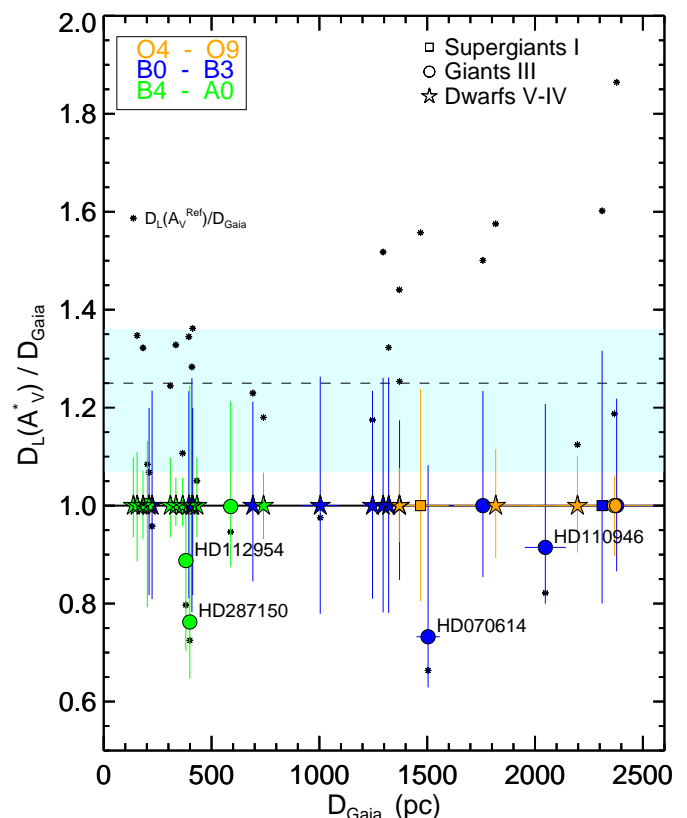

Fig. 5. Corrected distance ratios $D_L(A_V^*)/D_{Gaia}$ vs. D_{Gaia} (symbols in colour). The luminosity distance $D_L(A_V^*)$ was derived with our newly determined A_V^* utilizing Eq. 2 which brings the ratio to unity for all but four stars. The latter ones still agree within their errors with a ratio of one. For comparison unorrected distance ratios $D_L(A_V^{Ref})/D_{Gaia}$ of Fig. 1 are marked by dots.

8. Conclusion

We derive the visual extinction through the diffuse ISM from the trigonometric distance. We analyzed a critically selected sample of 33 nearby ($\lesssim 2.5$,kpc) early-type stars using the most comprehensive sample of reddening curves and SpL identification currently accessible. Our analysis uncovers, for 29 out of the 33 stars, a previously unknown micrometer-sized dust population. These account for 80 % of the sightlines studied. Due to its wavelength-independant extinction it is not seen in photometric data from the far UV – NIR range. The micrometer-sized dust component thus leads to an underestimate of the total dust content on the line of sight and – as a consequence – to significantly

larger distances when applying traditional photometric distance measurements.

The addition of a grey extinction component is the result of a physically consistent dust model, which incorporates micrometer-sized grains by satisfying the contemporary constraints of dust in the general field of the ISM (Hensley & Draine 2021), and includes an estimate of the visual extinction derived from the Gaia parallax. Our study emphasizes the significance of considering the absolute reddening of individual sightlines of the entire wavelength range and in particular in the NIR instead of utilizing the extrapolated parameter R_V. It underscores the necessity for further investigations of micrometre-sized dust particles in stellar distance determination. Along with its scattering properties (Witt & Gordon 2000; Scicluna et al. 2015), such a dust component in the vicinity of SNIa progenitors will contribute to the broadening of SN Ia light curves (Krügel 2015; Wang 2005), which has even implications for our understanding of the quantity of dark energy present in the universe (Riess et al. 1998).

References

Bagnulo, S., Cox, N. L. J., Cikota, A., et al. 2017, A&A, 608, A146
Bailer-Jones, C. A. L., Rybizki, J., Fouesneau, M., Demleitner, M., & Andrae, R. 2021, AJ, 161, 147
Bowen, D. V., Jenkins, E. B., Tripp, T. M., et al. 2008, ApJS, 176, 59
Chini, R., Krügel, E., Haslam, C. G. T., et al. 1993, A&A, 272, L5
Chini, R., Krügel, E., Lemke, R., & Ward-Thompson, D. 1995, A&A, 295, 317
Compiègne, M., Verstraete, L., Jones, A., et al. 2011, A&A, 525, A103
Das, H. K., Voshchinnikov, N. V., & Il'in, V. B. 2010, MNRAS, 404, 265
Dekker, H., D'Odorico, S., Kaufer, A., Delabre, B., & Kotzlowski, H. 2000, in Society of Photo-Optical Instrumentation Engineers (SPIE) Conference Series, Vol. 4008, Optical and IR Telescope Instrumentation and Detectors, ed. M. Iye & A. F. Moorwood, 534–545
Demyk, K., Gromov, V., Meny, C., et al. 2022, arXiv e-prints, arXiv:2209.06513
Deng, D., Sun, Y., Wang, T., Wang, Y., & Jiang, B. 2022, ApJ, 935, 175
Desert, F. X., Boulanger, F., & Puget, J. L. 1990, A&A, 500, 313
Draine, B. T. 2003, ARA&A, 41, 241
Draine, B. T. & Fraisse, A. A. 2009, ApJ, 696, 1
Draine, B. T. & Li, A. 2001, ApJ, 551, 807
Draine, B. T. & Li, A. 2007, ApJ, 657, 810
Dwek, E., Arendt, R. G., Fixsen, D. J., et al. 1997, ApJ, 475, 565
Fitzpatrick, E. L. & Massa, D. 2007, ApJ, 663, 320
Gaia Collaboration, Brown, A. G. A., Vallenari, A., et al. 2018a, A&A, 616, A1
Gaia Collaboration, Brown, A. G. A., Vallenari, A., et al. 2018b, A&A, 616, A1
Gaia Collaboration, Brown, A. G. A., Vallenari, A., et al. 2020, arXiv e-prints, arXiv:2012.01533
Galametz, M., Madden, S., Galliano, F., et al. 2009, A&A, 508, 645
Galliano, F., Madden, S. C., Jones, A. P., Wilson, C. D., & Bernard, J. P. 2005, A&A, 434, 867
Gordon, K. D., Cartledge, S., & Clayton, G. C. 2009, ApJ, 705, 1320
Gordon, K. D., Clayton, G. C., Decleir, M., et al. 2023, ApJ, 950, 86
Gray, R. O. & Corbally, C. J. 2014, AJ, 147, 80
Greenberg, J. M. & Chlewicki, G. 1983, ApJ, 272, 563
Guillet, V., Fanciullo, L., Verstraete, L., et al. 2018a, A&A, 610, A16
Guillet, V., Fanciullo, L., Verstraete, L., et al. 2018b, A&A, 610, A16
Heinz, S., Corrales, L., Smith, R., et al. 2016, ApJ, 825, 15
Hensley, B. S. & Draine, B. T. 2021, ApJ, 906, 73
Jones, A. P., Köhler, M., Ysard, N., Bocchio, M., & Verstraete, L. 2017, A&A, 602, A46
Jura, M., Webb, R. A., & Kahane, C. 2001, ApJ, 550, L71
Kennicutt, R. C., Calzetti, D., Aniano, G., et al. 2011, PASP, 123, 1347
Kharchenko, N. V. & Roeser, S. 2009a, VizieR Online Data Catalog, I/280B
Kharchenko, N. V. & Roeser, S. 2009b, VizieR Online Data Catalog, I/280B
Krełowski, J., Galazutdinov, G. A., Mulas, G., Maszewska, M., & Cecchi-Pestellini, C. 2015, MNRAS, 451, 3210
Krügel, E. 2008, An introduction to the physics of interstellar dust (IOP)
Krügel, E. 2015, A&A, 574, A8
Krügel, E. & Siebenmorgen, R. 1994, A&A, 288, 929
Krügel, E., Siebenmorgen, R., Zota, V., & Chini, R. 1998, A&A, 331, L9
Krüger, H., Strub, P., Grün, E., & Sterken, V. J. 2015, ApJ, 812, 139
Kyritsis, E., Maravelias, G., Zezas, A., et al. 2022, A&A, 657, A62

Landgraf, M., Baggaley, W. J., Grün, E., Krüger, H., & Linkert, G. 2000, J. Geophys. Res., 105, 10343
Lindegren, L., Bastian, U., Biermann, M., et al. 2021, A&A, 649, A4
Liu, Z., Cui, W., Liu, C., et al. 2019, ApJS, 241, 32
Luri, X., Brown, A. G. A., Sarro, L. M., et al. 2018, A&A, 616, A9
Madden, S. C., Rémy-Ruyer, A., Galametz, M., et al. 2013, PASP, 125, 600
Maercker, M., Khouri, T., Mecina, M., & De Beck, E. 2022, A&A, 663, A64
Maíz Apellániz, J. 2022, A&A, 657, A130
Mathis, J. S., Mezger, P. G., & Panagia, N. 1983, A&A, 128, 212
Mathis, J. S., Rumpl, W., & Nordsieck, K. H. 1977, ApJ, 217, 425
Mathis, J. S. & Whiffen, G. 1989, ApJ, 341, 808
Ormel, C. W., Min, M., Tielens, A. G. G. M., Dominik, C., & Paszun, D. 2011, A&A, 532, A43
Rémy-Ruyer, A., Madden, S. C., Galliano, F., et al. 2013, A&A, 557, A95
Riess, A. G., Filippenko, A. V., Challis, P., et al. 1998, AJ, 116, 1009
Scicluna, P., Siebenmorgen, R., Wesson, R., et al. 2015, A&A, 584, L10
Shull, J. M. & Danforth, C. W. 2019, ApJ, 882, 180
Siebenmorgen, R. 2023, A&A, 670, A115
Siebenmorgen, R., Krełowski, J., Smoker, J., Galazutdinov, G., & Bagnulo, S. 2020, A&A, 641, A35
Siebenmorgen, R. & Krügel, E. 1992, A&A, 259, 614
Siebenmorgen, R., Krügel, E., & Chini, R. 1999, A&A, 351, 495
Siebenmorgen, R., Scicluna, P., & Krełowski, J. 2018, A&A, 620, A32
Siebenmorgen, R., Smoker, J., Krełowski, J., Gordon, K., & Chini, R. 2023, A&A, 676, A132
Siebenmorgen, R., Voshchinnikov, N. V., & Bagnulo, S. 2014, A&A, 561, A82
Sota, A., Apellániz, J. M., Morrell, N. I., et al. 2014, A&AS, 211, 10
Trumpler, R. J. 1930, PASP, 42, 214
Valencic, L. A., Clayton, G. C., & Gordon, K. D. 2004, ApJ, 616, 912
Voshchinnikov, N. V. 2004, Astrophys. Space Phys. Res., 12, 1
Voshchinnikov, N. V., Il'in, V. B., & Das, H. K. 2016, MNRAS, 462, 2343
Wang, L. 2005, ApJ, 635, L33
Wang, S., Li, A., & Jiang, B. W. 2015a, MNRAS, 454, 569
Wang, S., Li, A., & Jiang, B. W. 2015b, ApJ, 811, 38
Wegner, W. 2006, MNRAS, 371, 185
Weingartner, J. C. & Draine, B. T. 2001, ApJ, 548, 296
Westphal, A. J., Stroud, R. M., Bechtel, H. A., et al. 2014, Science, 345, 786
Witt, A. N. & Gordon, K. D. 2000, ApJ, 528, 799
Witt, A. N., Smith, R. K., & Dwek, E. 2001, ApJ, 550, L201
Ysard, N., Jones, A. P., Guillet, V., et al. 2024, arXiv e-prints, arXiv:2401.07739